Improved representation of river runoff in Estimating the Circulation and Climate of the Ocean Version 4 (ECCOv4) simulations: implementation, evaluation, and impacts to coastal plume regions

Yang Feng[1,2,3], Dimitris Menemenlis[5], Huijie Xue[1,2], Hong Zhang[5], Dustin Carroll[6,5], Yan Du[1,2,4], Hui Wu[7]

1. State Key Laboratory of Tropical Oceanography, South China Sea Institute of Oceanology & Institution of South China Sea Ecology and Environmental Engineering, Chinese Academy of Science, Guangzhou, China
2. Southern Marine Science and Engineering Guangdong Laboratory, Guangzhou, China
3. Guangdong Key Laboratory of Ocean Remote Sensing, South China Sea Institute of Oceanology, Chinese Academy of Sciences
4. College of Marine Science, University of Chinese Academy of Sciences, Guangzhou, China
5. Jet Propulsion Laboratory, California Institute of Technology, Pasadena, California, USA
6. Moss Landing Marine Laboratories, San José State University, Moss Landing, California, USA
7. State Key Laboratory of Estuarine and Coastal Research, East China Normal University, Shanghai, China

Correspondence to: Yang Feng (yfeng@scsio.ac.cn)

Abstract

In this study, we improve the representation of global river runoff in the Estimating the Circulation and Climate of the Ocean Version 4 (ECCOv4) framework, allowing for a more realistic treatment of coastal plume dynamics. We use a suite of experiments to explore the sensitivity of coastal plume regions to runoff forcing, model grid resolution, and grid type. The results show that simulated Sea Surface Salinity (SSS) is reduced as the model grid resolution increases. Compared to Soil Moisture Active Passive (SMAP) observations, simulated SSS is closest to SMAP when using Daily, Point-source Runoff (DPR) and the intermediate-resolution LLC270 grid. The Wilmott skill score, which quantifies agreement between models and SMAP, yields up to 0.92 for large rivers such as the Amazon River. There was no significant difference in SSS for tropical and temperate coastal rivers when the model grid type was changed from ECCO v4 latitude-longitude-polar cap grid to ECCO2 cube-sphere grid. We also found that using DPR forcing and increasing model resolution from the coarse-resolution LLC90 grid to the intermediate-resolution LLC270 grid elevated the river plume area and volume, stabilized upper-layer stratification, and shoaled the mixed layer depth (MLD). Additionally, we find that the impacts of increasing model resolution from intermediate-resolution LLC270 grid to high-resolution LLC540 grid are regionally dependent. The Mississippi River Plume is more sensitive than other regions, possibly because the broader and shallower Texas-Louisiana shelf drives a more substantial baroclinic effect, and relatively weak sub-grid scale vertical mixing and adjustment in this region. Since rivers deliver enormous amounts of freshwater and anthropogenic materials to coastal areas, we believed that improving the representation of river runoff in global, high-resolution ocean models will advance studies of coastal hypoxia, carbon cycling, and regional weather and climate, and ultimately help to predict land-ocean-atmospheric feedbacks seamlessly in the next generation of earth system models.

1 Introduction

Coastal plume regions represent a small fraction of Earth's surface but play an active role in the global cycling of carbon and nutrients (Bourgeois et al., 2016; Carroll et al., 2020; Fennel et al., 2019; Lacroix et al., 2020; Landschützer et al., 2020; Roobaert et al., 2019). Recent satellite-based observations with quasi-global coverage have been greatly improved to monitor Sea Surface Salinity (SSS), a key tracer for tracking the river plumes. The European Space Agency (ESA) Soil Measure and Ocean Salinity (SMOS; Mecklenburg et al., 2012) with 33-km/10-day and National Aeronautics and Space Administration (NASA) Soil Moisture Active Passive (SMAP) missions with 40-km/8-day space/time gridding acquire SSS observations with sufficient resolution to track the plume pathways and to analyze the underlying dynamics (Fournier et al. 2016a, b; 2017a,b; 2019; Gierach et al. 2013; Liao et al., 2020). To date, however, coastal plume regions have not been explicitly resolved in most global Ocean General Circulation Models (OGCMs), Earth System Models (ESMs), and Global Ocean Data Assimilation System (GODAS) products (Ward et al., 2020). As a result, plume regions simulated by OGCMs, ESMs, and GODAS are not consistent with satellite observations. For example, Fournier et al. (2016a) found that the 1/12º global circulation Hybrid Coordinate Ocean Model (HYCOM) did not accurately capture SSS during extreme flood events in the northern Gulf of Mexico. Denamiel et al. (2013) found that the Congo River nearshore SSS in global HYCOM was underestimated compared to other regional simulations, even though the models had comparable horizontal grid resolution. Santini and Caporaso (2018) suggested that most CMIP5 models might lack skill in representing the Congo River Basin runoff and SSS in the vicinity of river mouths. Most OGCMs, ESMs, and GODAS products usually have large horizontal grid cells, and only a few cells may encompass the entire plume. As a result, freshwater delivered to these cells is thoroughly mixed and diluted, and therefore cannot represent the complex plume dynamics. Additionally, for the riverine freshwater input, the ocean is forced in the top model layer over a pre-determined surface area in the vicinity of river mouths, usually specified with a climatological signal. Thus, the system disturbances by extreme weather events, e.g., floods and droughts, cannot be explicitly resolved (Griffies et al. 2005; Tseng et al. 2016). Finally, virtual salt fluxes have been widely employed, where freshwater affects salinity without a change in mass or volume flux (Bentsen, 2013; Halliwell, 2004; Timmermann et al., 2009; Volodin et al., 2010). The above model configurations limit the representation of coastal plume region in global scale models.

Estimating the Circulation and Climate of the Ocean (ECCO) is a data assimilating model that uses observational data to make the best possible estimates of ocean circulation and its role in climate. The model uses the cube-sphere (ECCO2) and latitude-longitude-polar-cap (ECCOv4) grids for global application. Like most OGCMs, ESMs, and GODAS products, the current ECCO simulations route riverine freshwater from land directly to the ocean by using observed river runoff as a seasonal climatological mass flux over the top of several surface grid cells near the river mouths (Fekete et al. 2002; Stammer et al.2004). Recent ECCO efforts have been extended to address the global-ocean estimates of pCO_2 and air-sea carbon exchange (Carroll et al. 2020). The model resolution has been promoted as fine as 1-km globally to investigate mesoscale-to-submesoscale dynamics in the open ocean (Su et al., 2018). However, the current ECCO lacks representation of coastal interfaces and related feedbacks, which limits their application to global climate change and further impeding our ability to make informed resource management decisions. In this study, we here improved the representation of river runoff in ECCO and systematically evaluate model performance in reproducing SSS within the vicinity of large tropical and temperate river mouths. We also investigated the impact of runoff forcing, model grid resolution, and grid type on coastal dynamics and key plume physical properties. This work aims provide a comprehensive sensitivity analysis of runoff forcing in multiple simulations, which will help develop global ECCO simulations that more robustly represent the Land-Ocean-Aquatic-Continuum (LOAC).

The paper is organized as follows. Section 2 briefly introduces ECCO and the various runoff forcing methods used in this study. Section 3 provides a comprehensive evaluation of model sensitivity to horizontal grid resolution and river forcing. Section 4 discusses the sensitivity of plume properties and coastal stratification. Results are summarized in Section 5.

2 Methods

2.1 ECCO Simulations and Representation of River Runoff

In this study, we employ the Massachusetts Institute of Technology general circulation model (MITgcm; Marshall et al., 1997) in several model configurations developed for the ECCO project (Menemenlis et al., 2005; Forget et al., 2015; Zhang et al., 2018). The ECCO MITgcm configurations that we use herein solve the hydrostatic, Boussinesq equations on either Cubed Sphere (CS; Adcroft et al., 2004) or Latitude-Longitude-polar-Cap (LLC; Forget et al., 2015) grids. The cubed-sphere configuration is the so-called CS510 grid, which was developed for the ECCO2 project (Menemenlis et al., 2008), consisting of 6 faces with 510 × 510 dimensions. It has a quasi-homogeneous horizontal grid spacing of 20 km. We also consider three different LLC grid configurations: LLC90, LLC270, and LLC540, which have 1º, 1/3º, and 1/6º nominal horizontal grid spacing, respectively. The LLC grids are aligned with lines of latitude and longitude between 70° S and 57° N with grid spacing varing with latitude. We use LLC# horizontal grids for our experiments, where the # is the number of points along one-quarter of the equator. Therefore, LLC90 means 360 grid points circle the equator. The model has 50 vertical z-levels; the vertical resolution is 10 m in the top 7 levels and telescopes to 450 m at depth. This setup was the same for all designed experiments. We use a third-order, direct-space-time (DST-3) advection scheme, while vertical advection uses an implicit third-order upwind scheme. Vertical mixing is parameterized using the Gaspar-Grégoris-Lefevre (GGL) mixing-layer turbulence closure and convective adjustment scheme (Gaspar et al., 1990). Lateral eddy viscosity in ECCOv4 is harmonic, with a coefficient of $0.005L^2/\Delta t$, where L is the grid spacing in meters and $\Delta t = 3600s$. Depending on location, the resulting eddy viscosity varies from $\sim 10^3$ to $\sim 1.6 \times 10^4\ m^2 s^{-1}$. Additional sources of dissipation in ECCOv4 are from harmonic vertical viscosity and quadratic bottom drag, and contributions from the vertical mixing parameterization. A detailed description of ECCOv4 is provided in Forget et al. (2015).

ECCOv4 uses natural boundary conditions for both the river discharge and E-P (evaporation minus precipitation) (Huang 1993; Roullet and Madec; 2000). The runoff is applied as a real freshwater flux forcing, which allows for material exchanges through the free surface and more precise tracer conservation compared to virtual salt flux boundary conditions (Campin et al., 2008). The model uses z^* rescaled height vertical coordinates (Adcroft and Campin, 2004) and the vector-invariant form of the momentum equation (Adcroft et al., 2004). With z^* coordinates, variability in free surface height is distributed vertically over all grid cells. For a water column that extends from the bottom at $z = -H$ to the free surface at $z = \eta$, the z^* vertical coordinate is defined as $z = \eta + s^* z^*$, where $s^* = 1 + \eta/H$ is the rescaling factor. The Boussinesq, depth-dependent equations for conservation of volume and salinity under the vector-invariant form of the momentum equations are:

$$\frac{1}{H}\frac{\partial \eta}{\partial t} + \nabla_{z^*}(s^* v) + \frac{\partial w}{\partial z^*} = s^* F \qquad (1)$$

$$\frac{\partial (s^* S)}{\partial t} + \nabla_{z^*}(s^* S v_{res}) + \frac{\partial (S w_{res})}{\partial z^*} = s^*(D_{\sigma,S} + D_{v,S}) \qquad (2)$$

where F is the surface freshwater flux (includes both precipitation minus evaporation and river runoff), ∇_{z*} is the gradient operator on z^*plane. S is the potential salinity, $D_{v,S}$ and $D_{\sigma,S}$ are subgrid-scale processes parameterized as mixing diapycnal and along the isoneutral surface, which respect the highly adiabatic process of the oceanic interior (Griffies et al. 1998). The v_{res} and w_{res} are the horizontal and vertical residual mean velocity fields and hold the relationship $(v_{res}, w_{res}) = (v, w) + (v_b, w_b)$, where (v_b, w_b) is the bolus velocity parameterizing the effect of unresolved eddies (Gent and Mcwilliams, 1990). Our daily, point-source runoff (DPR) experiments add freshwater to a single model grid cell in the first vertical model layer, while the diffuse climatological runoff experiments add it over multiple horizontal grid cells in the top layer. The amount of freshwater added to each model grid cell decreases exponentially as a function of distance from river outlets.

2.2 Sensitivity Experiments

We first run seven experiments, derived from the ECCOv4 set-up, to test the sensitivity of SSS in the vicinity of large river mouths to ECCOv4 model grid resolution and runoff forcing (Table 1). The initial condition of ECCOv4 was from optimized adjustment of Mapping Ocean Observations in a Dynamical Framework: A 2004-06 Ocean Atlas (OCAA) and surface forcing was from adjustment of ECMWF Re-Analysis (ERA) interim. The LLC90, LLC270, and LLC540 corresponds to coarse (1° / ~100 km), intermediate (1/3° / ~40 km), and high (1/6° / ~20 km) resolution from low- to mid-latitudes, respectively. LLC90C and LLC270C are forced by monthly climatological runoff from Fekete et al. (2002). The runoff has a spatial resolution of ~1° and was linearly interpolated to each grid cell. Therefore, runoff may be fluxed into a single grid cell in the coarse-resolution run and over several grid cells in the high-resolution run. The twin experiments, LLC90R and LLC270R, the highest resolution run LLC540R, use Japanese 55-year atmospheric reanalysis (JRA55-DO) river forcing dataset (Suzuki et al., 2017; Tsujino et al., 2018). JRA55-DO includes daily river runoff is generated by running a global hydrodynamic model forced by adjusted land-surface runoff. Comparing to the Fekete ECCOv4 runoff, JRA55-DO runoff has daily output; therefore, it can resolve interannual variability and extreme floods and drought events. We add JRA55-DO runoff as point source flux at a single grid cell adjacent to river outlets for LLC90/270/540R. For the intermediate-resolution LLC270 run, we did two additional experiments: LLC270R_spread and LLC270R_clim. The LLC270R_spread used daily JRA55DO river discharge, but forced over several grid cells, which allows the model to automatically interpolate the runoff. The LLC270C_clim used single grid cell point-source surface forcing, but with climatological runoff derived from 2015–2017. The additional experiments were conducted because the widely-used climatological runoff by Fekete et al. (2002) in ECCOv4 differed from JRA55DO climatology. A comparison between LLC90C vs LLC270C, or LLC90R vs LLC270R vs LLC540R shows the resolution impacts. A comparison between LLC270R_spread and LLC270R shows the pure difference of adding runoff to a single grid cell (point-source runoff) vs multiple grid cell (diffusive runoff). In addition to the LLC grid, two additional experiments are conducted on the widely-used cube-sphere ECCO2 grid to investigate model sensitivity to the choice of grid topology (Table 1). CS510C is an ECCO2 run with monthly climatological runoff from Stammer (2004). The Stammer runoff is spread over a pre-determined surface area in the vicinity of river mouths. The spreading radius decreases exponentially with a 1000-km e-folding distance. Spatial fields of runoff forcing for ECCOv4, ECCO2, and JRA55-DO are shown in Figure S1.

#	Experiment Name	Grid Type	Runoff Forcing	Grid spacing
1	LLC90C	Lat-Lon-Cap	ECCOv4 Climatology	55–110 km
2	LLC90R	Lat-Lon-Cap	JRA55-do	55–110 km
3	LLC270C	Lat-Lon-Cap	ECCOv4 Climatology	18–36 km
4	LLC270R	Lat-Lon-Cap	JRA55-do	18–36 km
5	LLC270R_spread	Lat-Lon-Cap	JRA55-do	18–36 km
6	LLC270R_clim	Lat-Lon-Cap	JRA55-do	18–36 km
7	LLC540R	Lat-Lon-Cap	JRA55-do	9–18 km
8	CS510C (Standard ECCO2)	Cube-sphere	ECCO2 Climatology	~19 km
9	CS510R	Cube-sphere	JRA55-do	~19 km

Table 1: Summary of all experiments. The ECCOv4 and ECCO2 climatological runoff is derived from Fekete et al. 2002 and Stammer et al. 2004, respectively. A comparison of runoff forcing is shown in Figure S1.

Each sensitivity experiment is integrated for 26 years (1992–2017), and we analysed the final 3-year period (1 January 2015 to 31 December 2017). We begin our analysis in January 2015 because the high-resolution SMAP observations, which we use to evaluate model skill, are began on 1 April 2015. 10 large rivers at 8 coastal regions spanning from low- to mid-latitudes are selected for detailed analysis; including the Amazon and Orinoco (AZ), Congo (CG), Changjiang (CJ), Ganges and Brahmaputra (GB), Mississippi (MR), Parana (PA), Mekong (MK), and Columbia (CO) rivers **(Figure 1)**.

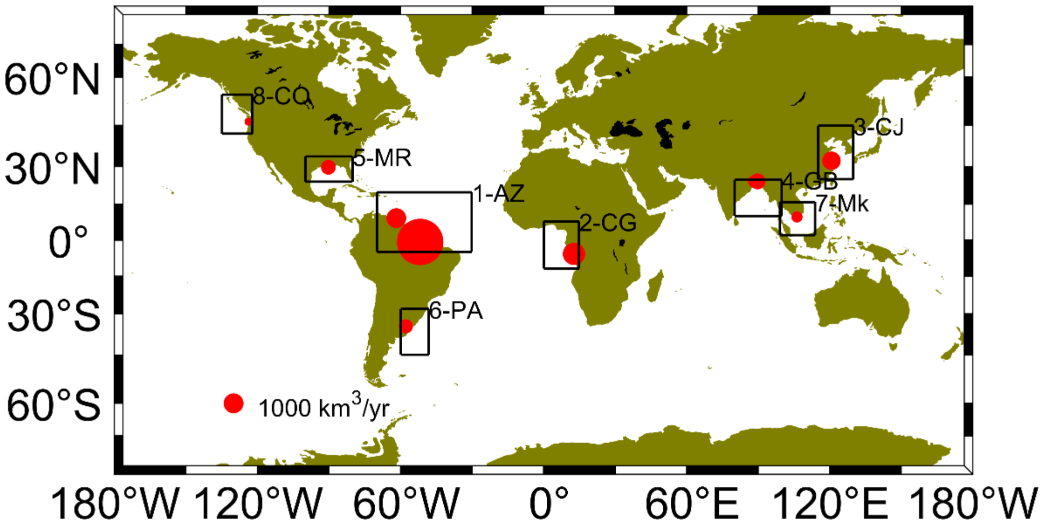

Figure 1: The 10 large rivers (red circles) at 8 coastal regions (black boxes) used in our analysis: Amazon and Orinoco (South America, noted as region 1), Congo (Africa, region 2), Changjiang (Asia, region 3), Ganges and Brahamptura (Asia, region 4), Mississippi (North America, region 5), Parana (South America, region 6), Mekong (Asia, region 7), Columbia (North America, region 8). Red circle size is scaled by the climatological river discharge magnitude.

2.3 Target Diagram and Willmott Skill Score

The first part of our study compares the simulated salinity with the synchronized SMAP SSS observations from 1 April 2015 to 31 December 2017 at the river mouth region (Section 3). The level 3 SMAP version-3 SSS was produced by the Jet Propulsion Laboratory (ftp://podaac-ftp.jpl.nasa.gov Yueh et al., 2013, 2014). We also compare climatological SSS during this period with the World Ocean Atlas 2018 (https://www.nodc.noaa.gov/OC5/woa18/). We use the Willmott skill score (Willmott, 1981), a widely-used metric for quantifying agreement between models and observations. The Willmott score is calculated as:

$$W_{skill} = 1 - \frac{\sum_{i=1}^{n}(M_i - O_i)^2}{\sum_{i=1}^{n}(|M_i - \bar{O}| + |O_i - \bar{O}|)^2} \qquad (3)$$

where M_i is the model estimate at t_i, O_i is the observation at time t_i, $\bar{O}$ is the mean of the observations, and n is the number of time records for comparison. Specifically, $W_{skill} = 1$ indicates perfect agreement between model and observations; $W_{skill} = 0$ indicates that the model skill is equivalent to the observational mean.

Furthermore, we conduct our skill assessment for model SSS on multiple experiments across several regions. We also use Target diagrams (Jolliff et al. 2009) to visualize a suite of skill metrics efficiently. Target diagrams are plotted in a Cartesian coordinate system with the x-axis representing the unbiased root-mean-square-deviation (RMSD), the y-axis represents the bias, and the distance between the origin and any point within the Cartesian space representing total RMSD.

$$Bias = \frac{\sum_{i=1}^{n}(M_i - O_i)}{n} = \bar{M} - \bar{O} \qquad (4)$$

$$\text{Unbiased } RMSD = \sqrt{\frac{\sum_{i=1}^{n}[(M_i - \bar{M}) - (O_i - \bar{O})]^2}{n}} \qquad (5)$$

$$RMSD = \sqrt{\frac{\sum_{i=1}^{n}(M_i - O_i)^2}{n}} \qquad (6)$$

$\bar{M}$ represents the mean of the model estimates. These three skill assessment statistics are particularly useful, as bias reports of the size of the model-observation discrepancies. Bias values near zero indicate a close match, though it can be misleading as negative and positive differences can cancel each other. The unbiased RMSD removes the mean and is a pure measure of how model variability differs from observational variability. The total RMSD provides an overall skill metric, as it includes components for assessing both the mean (bias) and the variability (unbiased RMSD).

We normalize the bias, unbiased RMSD, and total RMSD by the observational standard deviation (σ_0) to allow for the display of multiple experiment and regional SSS observations on a single Target Diagram. According to the definition of unbiased RMSD, the value should always be positive. However, the X < 0 region of the Cartesian coordinate space may be utilized if the unbiased RMSD is multiplied by the sign of the standard deviation difference (σ_d):

$$\sigma_d = sign(\sigma_m - \sigma_o) \qquad (7)$$

The resulting target diagram thus provides information about whether the model standard deviation is larger (X > 0) or smaller (X < 0) than the observations' standard deviation, in addition to if the model mean is larger (Y > 0) or smaller (Y < 0) than the observations' mean.

2.4 Definition of plume characteristics

We investigate the role of grid resolution and runoff forcing through several key metrics: plume area, volume, and freshwater thickness. The plume area is defined as regions with SSS below a given salinity threshold S_A (See Sect. 4.2). The freshwater volume, relative to the reference salinity, S_0, is defined as the integral of the freshwater fraction

$$V_f(S_A) = \iiint_{S<S_A} \frac{S_0 - S}{S_0} dV \qquad (8)$$

where the volume integral is bounded by the isohaline S_A. Here, we assume the maximum salinity in each selected region as the reference salinity S_0. The freshwater thickness δ_{fw} represents the equivalent depth of freshwater and is computed as:

$$\delta_{fw} = \int_{-h}^{\eta} \frac{S_0 - S}{S_0} dz \qquad (9)$$

$S(z)$ is the depth-dependent diluted salinity due to the river discharge, η is the sea level, and h is the bottom depth.

3. Comparison with SMAP and WOA18

We first estimate how various ECCOv4 LLC simulations (Table 1) compare to observations in the vicinity of 10 large river mouths. The synchronized SMAP SSS (01 April 2015 to 31 December 2017, 33-month) is used as the primary verification dataset (Yueh et al., 2013, 2014). SMAP SSS has been documented to exhibit bias compared to observed SSS in shallow waters near river mouths (Fournier et al., 2017). Therefore, as an indication of real SSS, we also compare the model simulations to the World Ocean Atlas 2018 (WOA18), which is an objective analysis of in-situ observations from a period of "climate normal" years (1981-2010) (Zweng et al., 2019). We note that there may be relatively few observations incorporated into the objectively-analysed WOA18 product near the coast, which may over-smooth salinity fronts. Additionally, WOA18 is a 55-year climatology from 1955–2010; therefore, we can only compare model climatology from 2015–2017. Overall, we use SMAP and WOA18 as "observational references", where our model-observation comparisons provide useful information on how SSS changes between experiments rather than determine which experiment is closer to the real world.

The upper 10-m SSS biases relative to SMAP, averaged over the 33 months, for CS510C (standard ECCO2) and the LLC540R (highest resolution) are shown in Figure S2. Both SMAP and WOA18 have 1/4° horizontal grid resolution, therefore, we interpolated all model fields to this grid. For both simulations, negative biases are found from low- to mid-latitudes, while positive biases occur at high latitudes. When focusing on large river mouth regions (e.g., AZ, PA, and CJ), the SSS bias is reduced in LLC540R. This demonstrates that the choice of runoff forcing impacts on SSS at predominantly local scales; however, background currents can transport the signal downstream or offshore to the open ocean (Liu et al., 2009; Molleri et al., 2010).

Next, we compute the mean model SSS near all selected river mouth regions, along with SMAP and WOA18 (Table 2). The corresponding Willmott Skill (WS) numbers are listed in Table 3. We use the 1st Empirical Orthogonal Function (EOF) derived from WOA18 to determine river mouth regions, since WOA18 represents persistent low-salinity zones over the 30 years. We remove the mean SSS field before the EOF analysis. The 1st mode explains ~47–67% of the total variance. We then reconstruct the dominant SSS anomaly field by multiplying the 1st PC with the spatial pattern. Locations with salinity that is 1~2 PSU lower in the reconstructed SSS field is taken as the river mouth region, and all eight regions are shown in Figure S3. The SMAP SSS has been found lower than the WOA18 SSS for large rivers. The underestimation is more than 5 PSU for the Amazon region. The deviation between satellite products and in-situ observations is consistent with Fournier et al. (2016) and Fournier et al. (2017). Near the selected large river mouths, experiments with daily, point-source runoff forcing have lower SSS than experiments forced by climatological diffusive runoff (LLC90R vs. LLC90C; LLC270R vs. LLC270C; CS510R vs CS510C). Increasing model resolution generally results in regions becoming fresher (Table 2; LLC90C to LLC270C; LLC90R to LLC270R to LLC540R). With the diffusive surface forcing, LLC270R_spread driven by daily JRA55DO has lower salinity than LLC270C driven by Fekete. This is not a surprise, since the model automatically interpolates the river forcing file to the model grids. The Fekete river discharge file spreads spatially more than JRA55DO before the model interpolation (Figure S1). This means less freshwater has been input to the top layer of the target river mouth region, resulting in a relatively high salinity. Moreover, with the daily JRA55DO forcing, the sea surface salinity with the point-source forcing (LLC270R) is lower than the diffusive forcing (LLC270R_spread). We can think about adding river to single grid cell instead of multiple cells was equivalent to decreasing the inlet width in regional models, which results in an increase in the inflow velocity, thus more efficiently spreading riverine freshwater within our selected river mouth area (Table 2). Lastly, our new runs show that with point-source river forcing, the runoff using year-by-year JRA55DO and climatological JRA55DO produced inconsistent SSS changes for selected rivers. Specifically, in the experiments with climatological JRA55DO, CG, CJ and PA river plumes have higher SSS, while AZ, GB, MR, MK and CO river plumes have lower SSS.

River Mouth	Abb.	Discharge (m^3/yr)	WOA 18	SMAP	LLC 90C	LLC 90R	LLC 270C	LLC 270R_spread	LLC 270R	LLC 270R_clim	LLC 540R	CS 510C	CS 510R
Amazon/ Orinoco	AZ	6440	32.7	27.5	34.0	34.1	31.7	30.4	28.2	27.6	24.6	34.3	23.8
Congo	CG	1270	33.6	33.7	34.7	34.3	34.6	35.3	33.9	35.2	33.7	34.9	34.1
Changjiang	CJ	907	32.9	31.4	33.1	32.8	33.0	33.2	32.2	32.4	31.8	32.5	30.9
Ganges /Brahamptura	GB	643	29.3	27.5	30.9	29.4	29.5	27.6	27.2	27.1	23.9	29.7	25.6
Mississippi	MR	552	33.5	34.8	35.8	34.7	35.8	34.4	34.1	33.3	33.8	35.3	34.1
Parana	PA	517	28.9	27.3	33.7	31.0	31.1	24.9	24.7	25.5	20.0	33.8	20.0
Mekong	MK	504	32.9	32.9	33.5	32.6	32.3	31.2	30.3	29.8	31.0	31.8	28.5
Columbia	CO	167	30.7	31.0	32.0	31.7	31.7	31.3	30.8	30.5	30.3	31.4	30.4

Table 2: The SSS near river mouth for WOA18, SMAP, and all experiments for the selected regions

A comparison with SMAP shows that W_{skill} scores become higher when model resolution increases from 1° to 1/3° (LLC90C vs LLC270C, LLC90R vs LLC270R), but lower when further increases to 1/6° (e.g., LLC270R vs LLC540R for Amazon, Ganges/Brahmaputra, Parana). The higher or lower W_{skill} score is consistent with the SSS decrease. In the AZ region, SSS from LLC270R is $\leq$1 PSU lower than the SMAP average, while LLC540R is ~3 PSU lower. Therefore, LLC270R receives a skill score of 0.92, higher than LLC540R (0.74). Although the SSS reduction lowers the model score overall, we should note that SMAP only has 1/4° resolution.This means it may not have the capability to resolve the fine-scale dynamic features of the plume compared to high-resolution model simulations. In addition, SMAP may underestimate SSS near the river mouth (Fournier et al. 2017). Therefore, a larger discrepancy with SMAP in high resolution run does not indicate the simulation deviates from the truth.

When taking SMAP as the reference, the W_{skill} scores show that LLC270R_spread is better than LLC270C for most rivers, such as AZ, GB, MR, PA, and CO. This is not surprising since the JRA55DO runoff has better temporal resolution compared to Fekete runoff. As a comparison, W_{skill} scores of LLC270R_spread is worse than LLC270R. This is because diffusive surface runoff results in higher SSS than point-source surface runoff (Figure S8).

When taking WOA as the reference, experiments forced with the climatological river forcing (LLC270R_clim and LLC270C) had better W_{skill} score than daily forcing runs (LLC270R_spread and LLC270R). This is can be expected since WOA is a climatological dataset. A comparison with SMAP score shows that most ECCO SSS products had comparable skills with SMAP, indicating that they are reliable to use as a climatological mean.

The higher or lower W_{skill} score is consistent with how much the model deviates from the observational reference. At the AZ region, SSS from LLC270R is less than 1 PSU lower than the SMAP average, while LLC540R is roughly 3 PSU lower. Therefore, LLC270R receives a skill score of 0.92, higher than LLC540R (0.74). This also occurs with LLC270C and LLC270R when using WOA18 as the reference.

For rivers in tropical and temperate zones, the CS510 grid has a resolution comparable with the LLC540 grid. Therefore, the SSS and skill scores are comparable between CS510R and LLC540R. Since the model grid type has a negligible impact on SSS for low- to mid-latitude rivers, we will discuss model sensitivity to runoff forcing and model grid resolutions only.

River Mouth	SMAP	LLC 90C	LLC 90R	LLC 270C	LLC270R_spread	LLC 270R	LLC270R_clim	LLC 540R	CS 510C	CS 510R
with SMAP										
Amazon / Orinoco	-	0.50	0.50	0.71	0.83	0.92	0.92	0.79	0.46	0.73
Congo	-	0.58	0.64	0.69	0.46	0.89	0.47	0.88	0.60	0.87
Changjiang	-	0.53	0.59	0.51	0.50	0.64	0.31	0.83	0.59	0.85
Ganges / Brahmaputra		0.61	0.71	0.69	0.83	0.85	0.84	0.69	0.57	0.70
Mississippi		0.55	0.79	0.53	0.75	0.77	0.69	0.75	0.49	0.72
Parana		0.37	0.51	0.45	0.60	0.62	0.56	0.40	0.37	0.40
Mekong		0.79	0.90	0.77	0.67	0.54	0.47	0.63	0.74	0.38
Columbia		0.46	0.60	0.49	0.68	0.73	0.70	0.74	0.27	0.61
with WOA										
Amazon / Orinoco	0.47	0.73	0.69	0.87	0.62	0.64	0.78	0.47	0.54	0.44
Congo	0.54	0.60	0.67	0.70	0.48	0.94	0.47	0.95	0.64	0.92
Changjiang	0.44	0.82	0.94	0.68	0.70	0.70	0.73	0.72	0.78	0.54
Ganges / Brahamptura	0.73	0.72	0.90	0.92	0.77	0.78	0.82	0.51	0.73	0.59
Mississippi	0.69	0.46	0.59	0.46	0.76	0.68	0.60	0.73	0.49	0.66
Parana	0.87	0.40	0.45	0.45	0.42	0.42	0.42	0.29	0.40	0.29
Mekong	0.64	0.84	0.87	0.83	0.39	0.45	0.59	0.54	0.71	0.30
Columbia	0.47	0.51	0.62	0.63	0.85	0.87	0.82	0.84	0.51	0.90

Table 3: The Willmott skill score for each run as compared with WOA18 and SMAP. The river mouth was recognized by the 1st EOF of WOA18 (See Figures 5 and S1). Note that WOA18 data are a 30- year climatology (1981—2010) and not in the same period as SMAP and experiments.

To better compare the sensitivity of SSS to river forcing, we provide zoomed-in plots of the same comparison shown in Figure 1 for AZ, MR, and CO Rivers for all LLC simulations, representing large, medium, and small rivers (Figure 2 and Figure S8). The positive bias is greatly reduced when applying daily, point-source river forcing, and increasing the horizontal grid resolution.

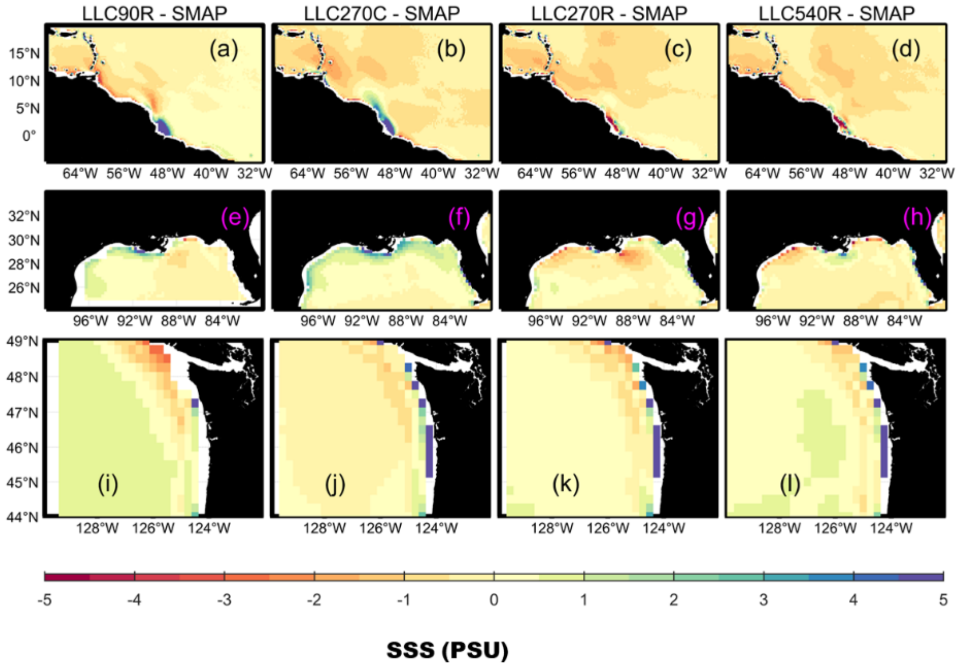

Figure 2: Zoomed-in view of SSS difference between model experiments and SMAP observations for large (Amazon, a–d), medium (Mississippi, e–h), and small (Columbia, i–l) rivers.

Timeseries for all LLC simulations and SMAP at these three river mouths, are shown in **Figure 3**. As in Figure 2, the bias decreases when daily, point-source river forcing is used and as the horizontal grid resolution increases. Additionally, the 2017 spring Amazon flood can be seen when forcing with diffusive daily JRA55DO (LLC270R_spread), but not by diffusive climatological Fekete case (LLC270C). The Mississippi/Columbia River mouth region is different from the Amazon in that the annual cycle of LLC270R_spread is stronger than LLC270C in all three years. This is because the seasonality of the Mississippi-Atchafalaya/Columbia River mouth has been oversmoothed in the climatological Fekete. The LLC270R_clim fluctuates in comparable with the LLC270R, except the annual extreme low SSS are comparable for the three simulated years.

Interestingly, the intermediate-resolution LLC270 run preforms better than the high CS510 resolution run in the Amazon region. This is because the Stammer et al. (2004) runoff is spatially smoother and lacks seasonal variability compared to the Fekete et al. (2002) runoff in this region (Figure S7). When using DPR forcing, the SSS differences associated with the river discharge interannual variability can be resolved as well. For example, the 2017 abnormally-low SSS near the Amazon river mouth is associated with an extreme flooding event (Barichivich et al., 2018).

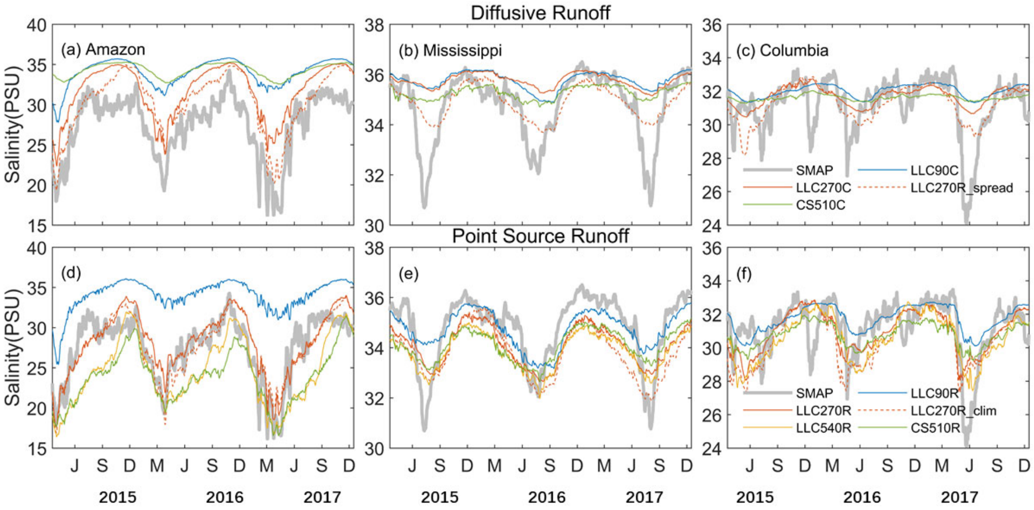

Figure 3: Area-averaged SSS in the Amazon, Mississippi, and Columbia river mouth regions (see Figure S3) with diffusive and point-source runoff forcing for SMAP (thick grey line) and experiments (thin coloured lines) with varying horizontal grid resolution. The method used to characterize the river mouth region is described in Section 3.

Next, we quantify the difference in mean and variance between the SSS time series of LLC simulations and that of SMAP using daily JRA55DO runoff but with diffusive and point source method for each **(Figure 4)**. With the same daily JRA55DO, the normalized bias has been found lower in the experiment with point sources than in the experiment with diffusive sources in general when forced with daily JRA55DO. The change in normalized unbiased RMSD is largely negligible compared to the changes in normalized bias for most rivers, except CG and MK. Most unbiased RMSD remains negative when switching the runoff forcing from climatological to daily for most regions. This implies that the variance of LLC simulations remains lower than SMAP observations despite of the runoff forcing changes. The exception of the CG River is possibility because it is a near equator eastern boundary plume where freshwater transport distinguished from others (Palma and Matano, 2017), and the abnormal MK may reflect SMAP data are contaminated by the land signal near Vietnam coast, introducing lots of noise to the SSS timeseries.

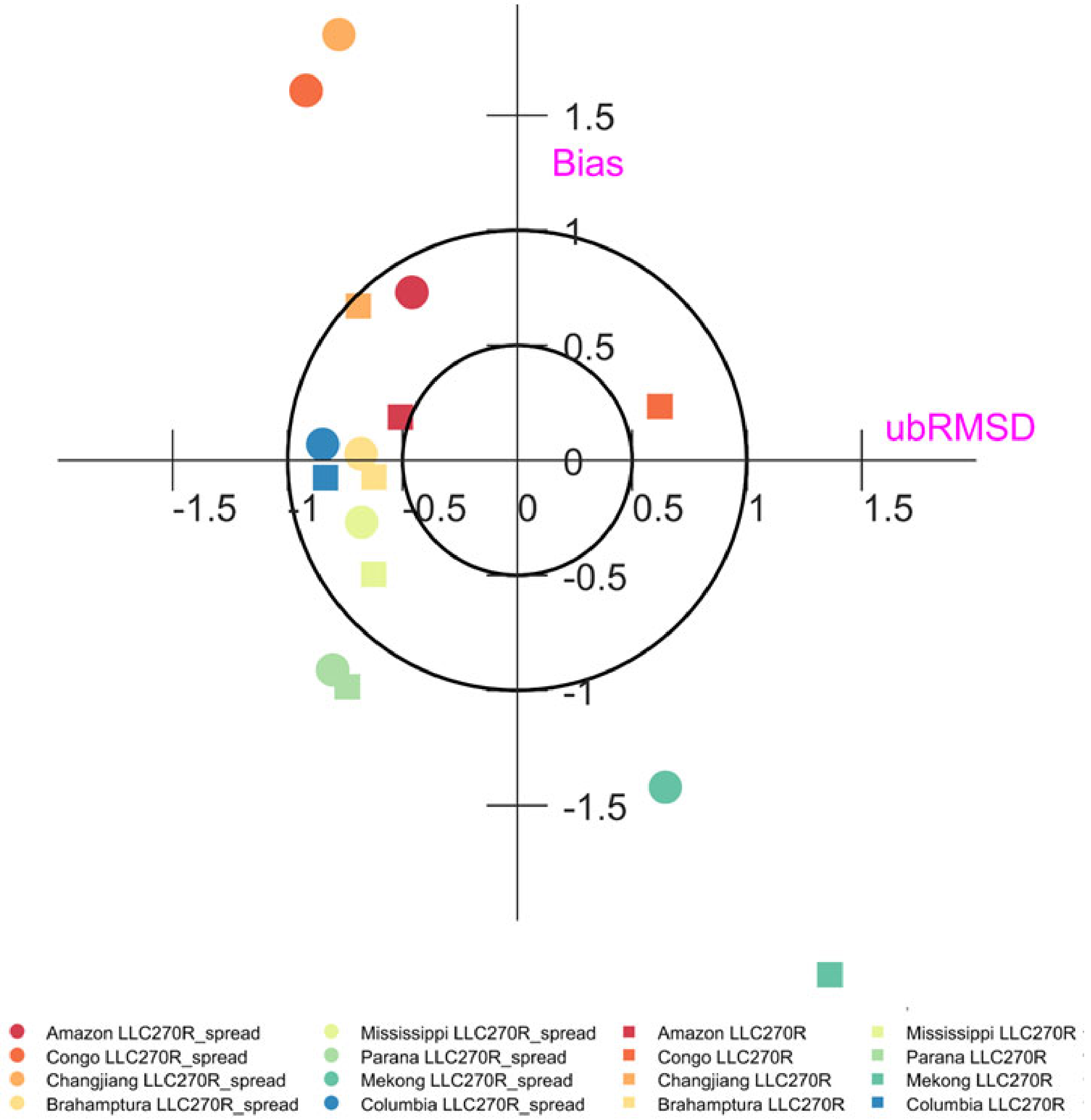

Figure 4: SSS target diagram near the selected river mouths (see Figure S3) for LLC270R_spread and LLC270R simulations.

We also examine the bias and variance on the Target Diagram for experiments with varying grid resolution but similar daily runoff forcing **(Figure 5)**. Our results show that the normalized bias decreases as the model resolution increases, which is consistent with the SSS reduction in Table 2 and relatively low W_{skill} in Table 3. The unbiased RMSD decreases slightly, with the sign remaining negative as the model resolution increases. This occurs everywhere, except for the two largest rivers (AZ and CG) where the sign becomes positive for LLC540R, indicating that the model variance exceeds the SMAP variance when using the high-resolution grid. In summary, the comparison with synchronized

SMAP shows that using daily runoff and finer horizontal grid resolution improves the representation of SSS variability but at a cost of increased SSS bias.

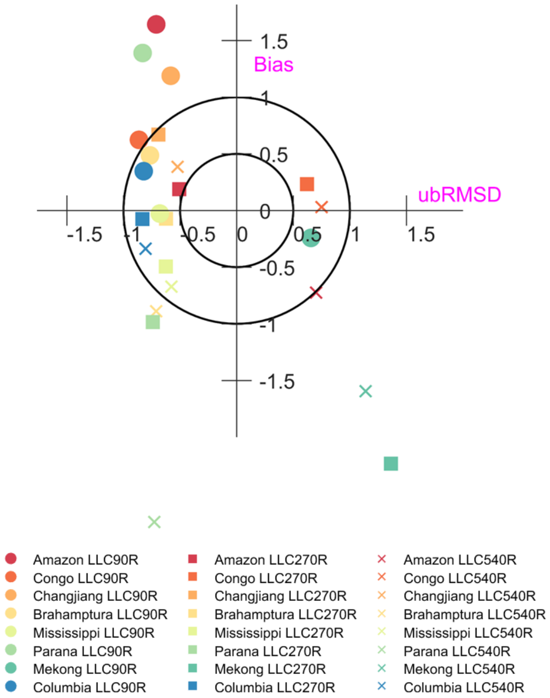

Figure 5: Same as Fig. 4, but for LLC90R, LLC270R, and LLC540R.

4. Impact on River Plume Properties

4.1 EOF analysis of SSS

We next investigate how model runoff improvements impact river plume properties such as plume area, volume, and freshwater thickness. Here, we focus on how the widely-used ECCOv4 simulation (forced by Fekete runoff) is different from the new DPR implementation. We limit our discussion to LLC#C/R cases only (Exp. 1, 2, 3, 4 and 7). We first evaluate plume SSS signature and dynamics through EOFs; the mean is removed before the EOF analysis. The first and second mode of AZ, MR, and CO using the same grid resolution but with different runoff forcing is shown in Figures 6 and S4. The spatial pattern reveals the salinity anomaly caused by the runoff, while the PC timeseries shows the timing. A single value in the spatial pattern or PC timeseries doesn’t have an exact physical meaning, but together they reveal how much salinity deviates from the mean. The PC timeseries for experiments with DPR forcing clearly show similar seasonal cycles, albeit with larger amplitudes and interannual variability.

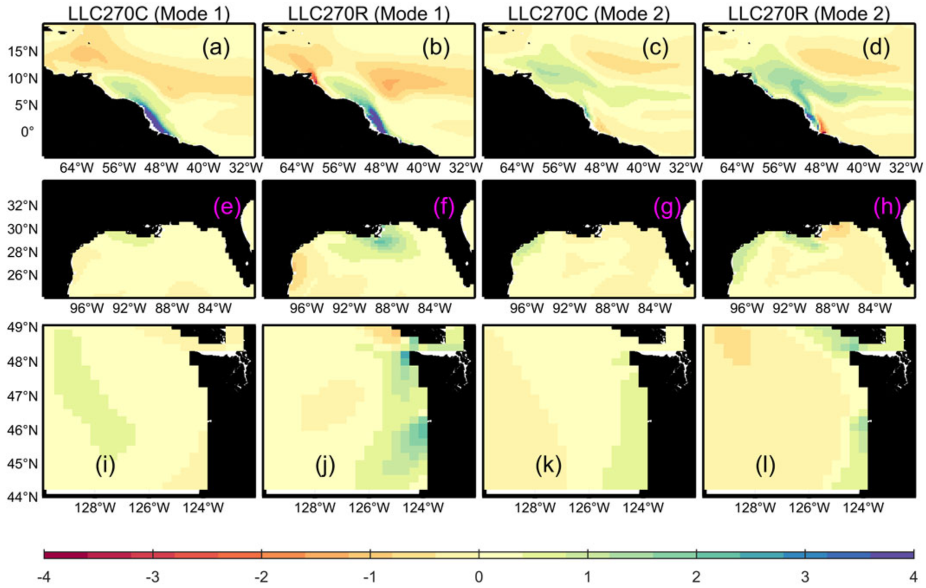

Figure 6: 1st and 2nd EOF spatial patterns from the LLC270C and LLC270R simulations for the Amazon, Mississippi, and Columbia rivers. The corresponding PC timeseries are normalized by the standard deviation and multiplied with the spatial mode.

For the AZ region, the LLC270R and LLC270C spatial patterns are similar for the first and second mode. The first mode accounts for 59% (72%) of the total variance in LLC270R (LLC270C). The spatial pattern reveals a low-salinity tongue; which located in a narrow band along the north-eastern South American coast from February–June, which is associated with the large river discharge and the northward-flowing North Brazil Current. The second mode of LLC270R (LLC270C) accounts for 33% (23%) of the total variance. The spatial pattern shows that the plume-like features extend northwestward to the Caribbean Sea and Central Equatorial Atlantic Ocean from May–September. This pattern is driven by Ekman currents associated with northeasterly wind stress and the transport to the Central Equator is due to the North Equatorial Counter Current (NECC, Lentz 1995a, b).

For the MR region, the first and second mode of LLC270R (LLC270C) explains 53% (66%) and 29% (18%) of the total variance, respectively. The spatial pattern of the first mode is generally similar. There is a bulge-like plume feature that occupies a region near the MR mouth with a southeast extension to the central Gulf of Mexico from May–October (Figure S4), while the freshwater signal in the vicinity of the southeast MR mouth is stronger in LLC270R. The extension of low-salinity waters is due to the upwelling-favourable winds (southwesterly) from late-spring to summer, which transport the MR freshwater offshore (Walker, 1996). The spatial pattern of the second EOF mode represents the low salinity Mississippi River plume water transport downcoast from Louisiana towards Texas, which is carried by the reversed shelf circulation from September to May (Cochrane and Kelly, 1986).

The first and second mode explains 63% (56%) and 29% (33%) of the variability at the CO region in LLC270C (LLC270R), respectively. It has been previously recognized that the CO plume exhibits seasonal variability forced by wind and freshwater discharge (García Berdeal *et al.*, 2002). During winter, Ekman transport resulting from the northward winds constrains the plume against the Washington coast. Downwelling-favorable wind stress strengthen the anti-cyclonic rotation of the river plume, resulting in a coastally-attached winter plume. In contrast, prevailing southward wind stress results in offshore Ekman transport; this advects the plume offshore, where it is influenced by the California Current over long timescales and subsequently veers southward and offshore (Banas et al., 2009). This seasonal pattern is shown in the first LLC270R mode and second LLC270C mode.

The first and second EOF modes for AZ, MR, and CO with daily runoff forcing in coarse (LLC90R) and fine (LLC540R) grid resolution are shown in Figures 7 and S5. The plume-like features and associated dynamics are similar to LLC270 in both runs. Additionally, the higher-resolution LLC540R resolves fine-scale plume structure for several major rivers, which was previously revealed by satellite observations, regional simulations, or neural network methods (e.g. meanders and rings of the AZ plume due to the North Brazilian Current (NBC) retroflection, Molleri et al. 2010). In LLC540R, "horseshoe" patterns of the MR plume are associated with Texas floods (Fournier et al. 2016), and the bidirectional CO plume is seen during variable summer wind patterns (Liu et al. 2009). Overall, EOF SSS analysis shows that general plume patterns and dynamics are grid independent; however, fine-scale plume structures are only resolved by high-resolution simulations.

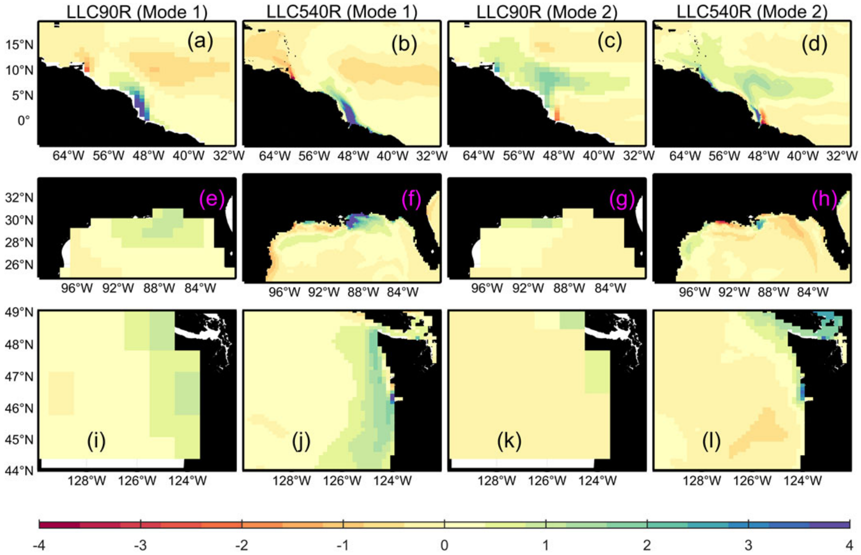

Figure 7: Same as Fig. 6 but for the LLC90R and LLC540R simulations. The corresponding PC timeseries are normalized by the standard deviation and multiplied with the spatial mode shown in Figure S5.

4.2 Plume Area, Volume, and Freshwater Thickness

We first calculated the plume area using the salinity threshold from 28 to 36 PSU. The 3yr-average plume area for AZ, MR, and CO river region for different LLC configurations is shown in Figure 8. Under either the climatological diffusive or DPR river forcing, we could see the plume area increasing when model resolution increase from 1° to 1/3° for all regions. While the plume area responds to the model resolution change to 1/6°, this can only can be seen in the Mississippi River region. To highlight the seasonal and interannual variability are at the given threshold, we also show the plume area and volume within $S_A = 30$ PSU using climatological and daily runoff forcing in the coarse-, intermediate-, and high- resolution runs (Figures S6, 9). Figure 9 presents a time series of freshwater volume within the given salinity during this period. There is a stronger interannual variability when using DPR, and larger plume area and volume during flood years. The MR and CO plume area/volume cannot be explicitly resolved at the $S_A = 30$ threshold when using the climatological and runoff forcing, since river runoff has been distributed over broad spatial grids and surface salinity decrease is small. For the AZ region, the averaged plume area (volume) approaches 6 × 10^4 km^2 (7 × 10^2 km^3) in LLC270C, whereas it is only about 3 × 10^4 km^2 (5 × 10^2 km^3) in LLC90C. In contrast, the MR and CO plume area (volume) is easily recognized when using DPR forcing. The AZ plume increases as the grid resolution increases, reaching 10, 13, and 17 × 10^4 km^2 in LLC90R, LLC270R, and LLC540R, respectively. The freshwater volume in coarse-, intermediate-, and high-resolution runs is comparable, with values of ~ 1.5 - 2 × 10^2 km^3. The plume area and volume in the MR region is more sensitive to the model grid resolution than AZ and CO. The LLC540R plume area is ~3–4 times larger than LLC270R, while LLC270R is ~6–7 times larger than LLC90R. When using DPR forcing, the CO region's plume area is similar between intermediate- and fine-resolution experiments, with the area in LLC270R and LLC540R increasing to ~1 × 10^5 km^2 during the 2015 flood year. In contrast, LLC540R maintains a larger plume volume than the intermediate resolution run.

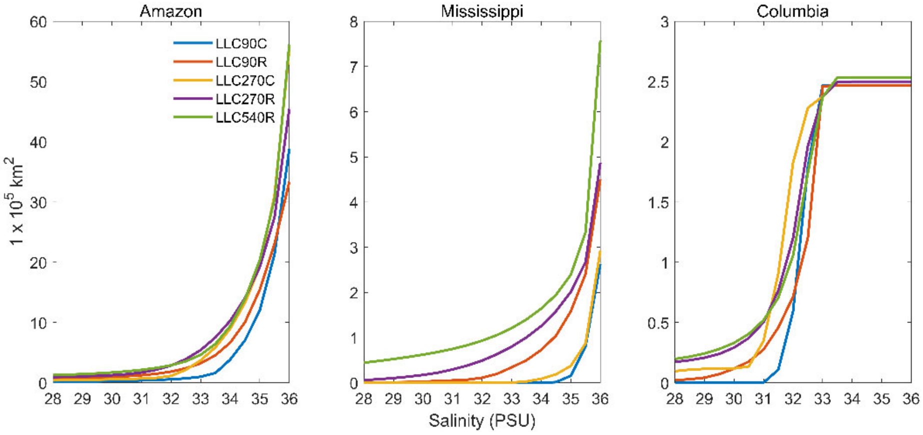

Figure 8: 2015-2017 averaged plume area at salinity threshold S_a from 28 to 36 for the Amazon, Mississippi, and Columbia River regions.

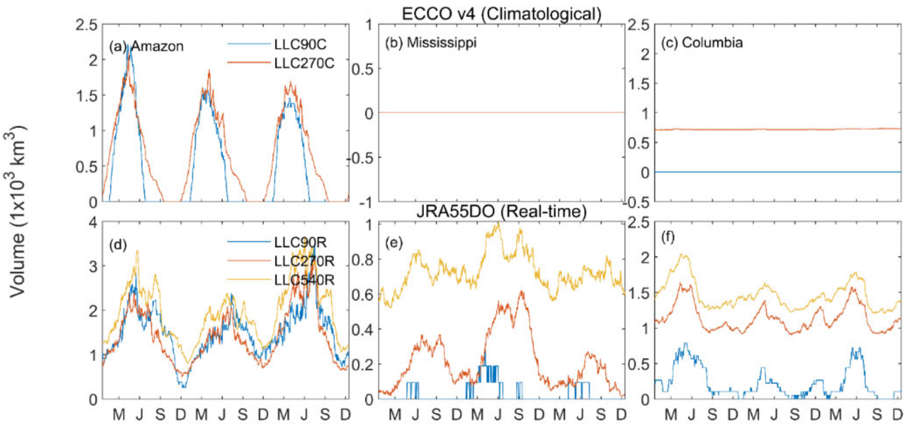

Figure 9: Freshwater volume within 30 PSU for the Amazon, Mississippi, and Columbia river regions for various experiments; reference salinity is 36 PSU.

The sensitivity of plume area and volume to runoff forcing and grid resolution reflects the experiment's ability to resolve horizontal advection and downward mixing of riverine freshwater. This can be partially reflected in the freshwater thickness calculation, which is shown in Figure 10. For the intermediate resolution experiments, the maximum freshwater thickness δ_{fw} is over 10 m, 5 m, and 4 m near the AZ, MR, and CO river mouths when using DPR, as opposed to 4 m, 2 m, and 2 m, when using climatological runoff. Additionally, the freshwater thickness in experiments with DPR but different grid resolutions (LLC270R and LLC540R) demonstrates that a coherent plume rotates and responds to external wind and background flow; this coastal plume structure is largely absent in the coarser LLC90R. The coarse-resolution experiment exhibits a more diffuse response, with lower salinity near MR and CO river mouths. Note that the runoff forcing is identical between LLC90R, LLC270R, and LLC540R experiments, and differences in plume area, volume, and freshwater thickness are due to model resolution alone. The freshwater flux in the higher resolution experiments can result in larger inflow velocities, a more robust baroclinic response, and a more vigorous coastal plume. The plume area and volume in MR region are more sensitive to grid resolution — this possibly results from the representation of shelf bathymetry. The Texas-Louisiana shelf is wider and shoals more gradually from the coastline than the northern Brazilian shelf (AZ) and Washington shelf (CO). When adding the same amount of freshwater in shallow water regions, high resolution experiments generate a larger pressure gradient force than the intermediate resolution, which drive more substantial baroclinic effect and elevate coastal currents. The alongshore currents can advect the MR Plume water downcoast, which enlarges the plume area. Additionally, plume waters may be entrained downward by strong sub-grid vertical mixing and adjustment, e.g., meso-scale eddies, when flowing offshore to the open ocean as the horizontal resolution increases from intermediate to high. The eddies in high resolution run at AZ and CO may also break up the plumes and reduce their area compared to low-to-intermediate resolution runs (Figure 8).

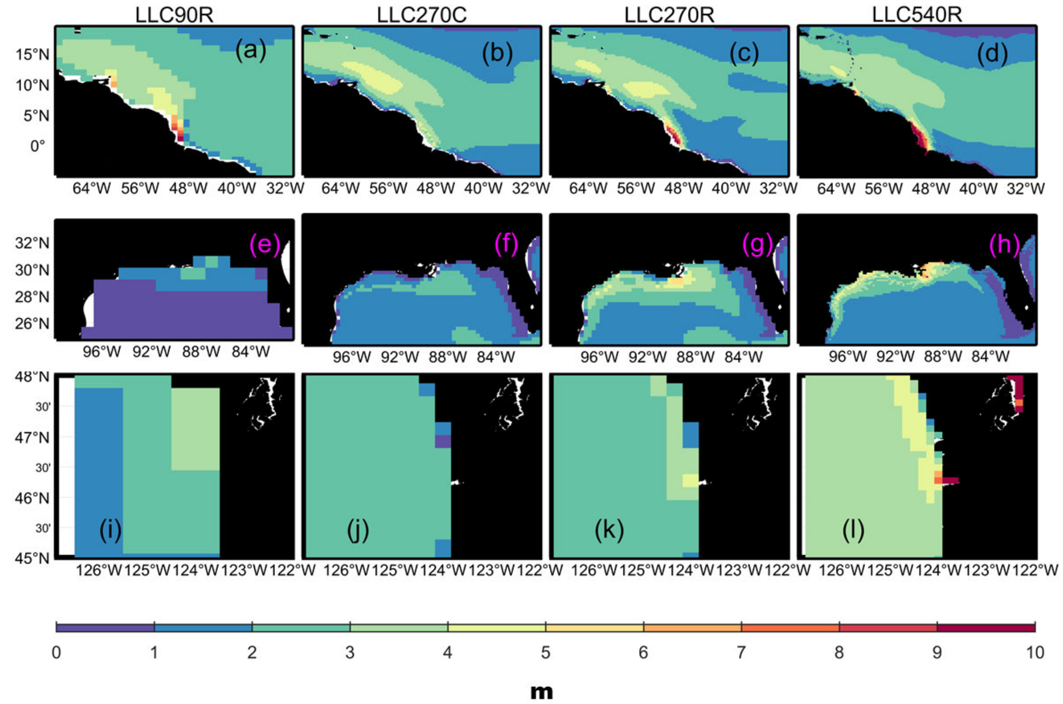

Figure 10: Freshwater thickness for the Amazon, Mississippi, and Columbia river regions in LLC90R, LLC270C, LLC270R, and LLC540R experiments.

4.3 Impact on Ocean Properties Associated with SSS

This section examines the sensitivity of stratification and mixed layer depth (MLD) between different experiments. Figure 11 shows 3-year averaged vertical profiles of salinity, temperature, vertical density gradient $d\rho/dz$ (ρ is the potential density) near the AZ (top), MR (middle), and CO (bottom) river mouths, respectively. The profiles are averaged over the horizontal regions shown in Figure S3. The vertical density gradient is an important indicator of stratification strength. The salinity differences between climatological (LLC90/270C) and DPR forcing (LLC90/270R) are large near the surface and diminish with increasing depth. The temperature difference when using the two types of runoff forcing is insignificant, demonstrating that the stratification difference is primarily determined by salinity and the addition of freshwater. Additionally, DPR forcing greatly increases subsurface stratification, which implies a decrease in vertical mixing.

Figure 11 also shows the sensitivity of upper-ocean stratification to various model grid resolutions. The profiles show a significant decrease in salinity from the surface to 50-m depth as the resolution increases, impacting the stratification (rightmost panels). We note that the vertical density gradient has a subsurface maximum in the coarse- and intermediate-resolution run. In contrast, the high-resolution experiment has a surface maximum due to low-salinity water concentrated in the surface level. SST is highest in LL540R at AZ and MR, reflecting that heat is preserved at the surface due to the increase in subsurface stratification.

The sensitivity of stratification in the above analysis implies that the MLD can be altered by river forcing and grid resolution. We compare the MLD in the vicinity of AZ, MR, and CO during the simulation period in Figure 12. The MLD in our calculation uses the threshold method, in which deeper levels are examined until one is found with a density differing from the near surface by more than 0.03 kg/m^3 (de Boyer Montégut et al., 2004). This reflects the maximum depth of the boundary layer that is sustained by riverine freshwater. Interestingly, all experiments simulate the annual cycle of MLD. There was relatively shallow MLD from April to December, which corresponds to periods of high river discharge. The MLD in the DPR forcing and high-resolution scenario is shallower than the climatological, low-resolution scenario, which is consistent with vertical salinity and stratification profiles shown in Figure 11.

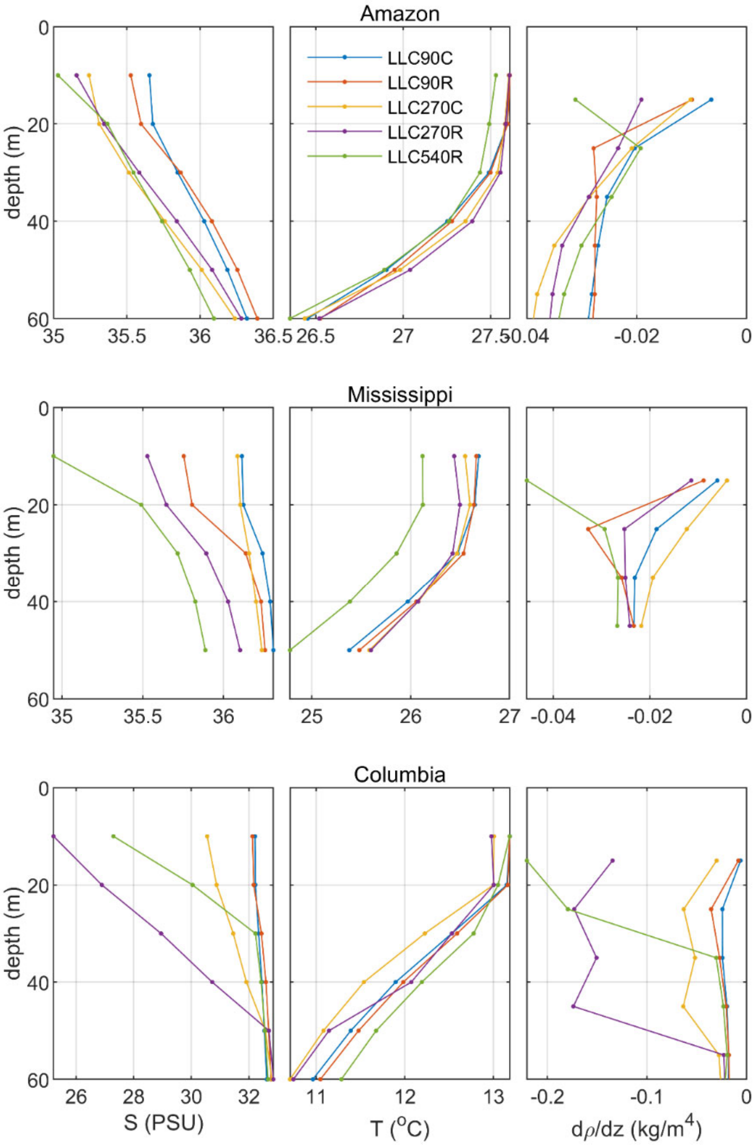

Figure 11: Mean 3-year (2015-2017) salinity, potential temperature, and vertical density gradient ($d\rho/dz$) profiles.

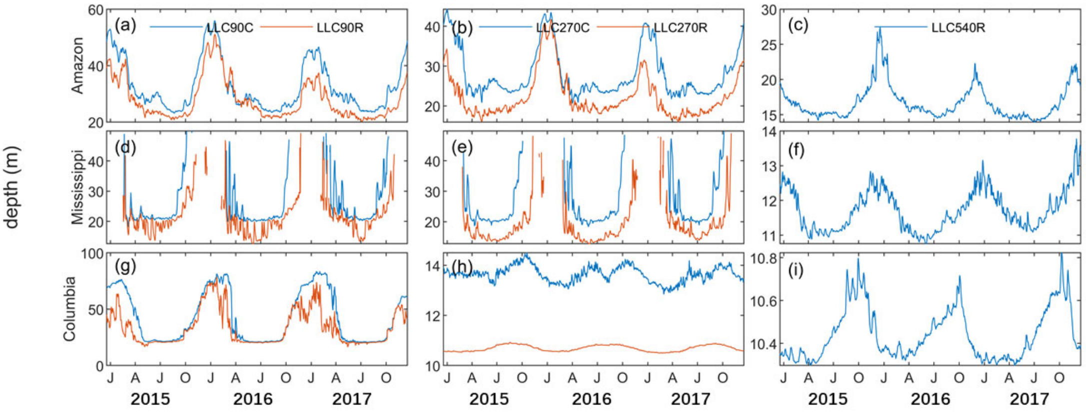

Figure 12. 2015–2017 daily MLD, averaged in the vicinity of the Amazon River (upper panels), Mississippi River (middle panels), and Columbia River (lower panels) mouth. MLD is computed as done in Boyer Montegut et al. (2004).

5. Discussion and conclusions

This study investigates the model sensitivity of runoff forcing and grid resolution and type under the ECCO framework. We find that DPR significantly improves model representation of global rivers, with horizontal model resolution having a substantial control on SSS in the vicinity of river mouths. We observe no significant changes in tropical and temperate river mouth SSS when using cube sphere grid vs LLC grid types when using the same river forcing. A comparison with synchronized SMAP observations shows that the use of DPR forcing and intermediate grid resolution can increase the model performance in simulating SSS in the vicinity of river mouths. However, further increasing model grid resolution from intermediate to high may result in an additional SSS bias towards fresher values.

Previous theoretical modelling studies have demonstrated that, in the absence of external forcing, large river plumes influenced by rotational effects tend to veer anticyclonically and form a bulge region near the river mouth as well as an along-shore downstream coastal current as Kelvin waves (Kourafalou et al. 1996; Yankovsky and Chapman, 1997). Additionally, idealized numerical simulations have revealed that river plume behaviour is greatly impacted by external forcing. Chao (1988a, b) demonstrated that vertical mixing, bottom drag, and bottom slope greatly impact the spin-up, maintenance, and dissipation of river plumes. Fong and Geyer (2001) revealed that a surface-trapped river plume would thin and be advected offshore by cross-shore Ekman transport. Additionally, Fong and Geyer (2002) suggested that the ambient current, which is in the same direction as the geostrophic coastal current, can augment plume transport. Our ECCO experiments examine the above river plume theoretical results globally with realistic topography and external atmospheric forcing. Our EOF analysis of SSS at the AZ, MR, and CO shelves shows that the general plume spatial and temporal patterns related to river discharge, wind, and currents are independent of the grid resolution and forcing formulations, which are consistent with previous theoretical studies. However, higher resolution and DPR forcing may be vital for resolving the small rivers' fine-scale plume dynamics. Using DPR forcing and increasing the model grid resolution from coarse to intermediate increases the river plume area and volume, while further increasing the model resolution from intermediate to high has mostly regional effects. Shallow and wide shelf regions, such as the Mississippi Delta, are more sensitive to the model resolution compared to AZ and CO. Recent increases in computational power have allowed GODAS products, such as ECCO, to provide model output at different resolutions, which supports regional scientific studies using offline methods (e.g. the Lagrangian method, Meng et al. 2020; Liang et al. 2019). Our results suggest that how high-resolution products should be used depends on the relevant spatio-temporal dynamics and geomorphologic characteristic of the studied region. We also found that using DPR forcing and increasing the model grid resolution can stabilize the water column at the subsurface and shoal the MLD. This may have significant implications for biogeochemical cycles and air-sea exchange in coastal zones. From the biogeochemistry perspective, riverine freshwater increases shelf stratification, which can prevent reoxygenation of bottom waters and thus can result in large hypoxic regions (Fennel, et al. 2011; Feng et al. 2019). From the air-sea interaction perspective, on one hand, SST can trigger deep atmospheric convection and intense rainfall. On the other hand, strong near-surface stratification may inhibit cooling and intensify tropical cyclones (Cione and Uhlhorn, 2003; Neetu et al., 2012; Rao and Sivakumar, 2003; Sengupta et al., 2008; Vialard & Allison et al., 2000; Vinaychandran et al., 2002). We envision that future work investigating river impacts on ocean-atmospheric and earth system dynamics could be accomplished by coupling our improved ECCO simulations with an atmospheric general circulation model (AGCM).

In the state-of-art OGCMs, ESMs, and most GODAS products, river runoff is incorporated on coarse resolution grids as augmented precipitation. Climatological runoff forcing is often used in conjunction with artificial spreading and a virtual salt flux scheme. Tseng et al. (2016) examined model sensitivity to the spreading radius, turbulent mixing parameterization, reference salinity, and vertical distribution of riverine freshwater on 1° resolution in Community Earth System Model (CESM). For all factors examined, they found that the model results are most sensitive to the spreading radius, which substantiates the importance of our finding that the associated plume properties, including the area hence the SSS near river mouths exhibit strong responses when switching the runoff flux from diffusive climatological to daily point-source.

The present state-of-the art regional scale estuarine models can simulate estuarine hydrodynamics and biogeochemical processes in a robust manner. The inlet approach, which defines a rectangular breach in coastal land cells with uniform density and discharge, is widely used (Herzfeld, 2015; Garvine, 2001). An additional barotropic pressure term may be added to account for pressure gradients induced by the freshwater plume (Schiller and Kourafalou, 2011). The inlet approach has also been used in global z-coordinate models by injecting freshwater in multiple vertical grid cells (Griffies et al. 2005). In our simulations, sea level changes are redistributed over-all vertical grid cells by the rescaled height vertical coordinate. This is similar to the inlet approach in the regional models, which add a mass or volume flux of freshwater to a breach in coastal land cells (Garvine 1999). Herzfeld (2015) investigated the role of model resolution on plume response at the Great Barrier Reef (GBR) using the Regional Ocean Modeling System (ROMS). The study found that the plume veered left and followed a northward trajectory to Cape Bowling Green in a 1 km resolution model but not in a 4 km resolution model. Our findings are consistent with this result. The plume properties in our intermediate resolution simulations are more clearly detected than in the coarse resolution simulations. Our results also expand on their findings by showing that the sensitivity of plume properties in high resolution model is highly-dependent on shelf bathymetry. Schiller and Kourafalou (2010) investigated the dynamics of large-scale river plumes in idealized numerical experiments using HYCOM to address how the development and structure of a buoyant plume are affected by the vertical and horizontal redistribution of river inflow and bottom topography. Their experiments show that a narrow inlet, flat bottom facilitates a larger right-turning plume bulge region than a wide inlet, slope bottom (see their Figure 8 Riv2c-f; Riv2c-s). This is complementary to our findings that the MR plume, located on the wide and shallow LA shelf, has a larger horizontal plume area than the AZ and CO plume when increasing the horizontal resolution from intermediate to high. However, their discussion was limited to an idealized, rectangular model domain without external forcing, while our model simulations provide a practical application to natural river plume systems. The global application of the regional inlet representation of river forcing was also used by NOAA's Geophysical Fluid Dynamics Laboratory (GFDL) models (Griffies et al., 2005). An internal, pre-computed salinity source term was introduced into multiple vertical layers. However, river representation was done through virtual salt flux rather than through real mass or freshwater volume flux. Adding the real volume and mass of freshwater through multiple layers has been widely used in regional models like ROMS; it may be useful to adapt this technology into future ECCO simulations and compare the results with the current surface injection methods.

For the global ocean, river runoff is much smaller than the precipitation and evaporation flux; therefore, it is parameterized for most OGCMs, ESMs, and GODAS products. One of the most significant expected signatures of global warming is an acceleration of the terrestrial hydrological cycle (IPCCs, 2019; Piecuch and Wadehra, 2020). Both can significantly affect the magnitude, distribution, and timing of global runoff, leading to extremes in the frequency and magnitude of floods and droughts. When considering water resource management issues under climate and land use/land cover change, a key question such as "how will coastal oceans be impacted from flood and drought events?" is challenging to answer (Fournier et al., 2019). In the future, high-resolution global-ocean circulation models with DPR forcing may help identify the primary forcing mechanisms, such as those from climate-driven extreme events, which drive variability of large river plume systems just as skillfully as a regional model set-up.

Improved model representation of rivers may not be as important for global or basin- scale hydrological cycles as precipitation and evaporation (Du and Zhang, 2015), but may be critical for the global carbon cycle (Friedlingstein et al., 2019; Resplandy et al. 2018). River delivers large amounts of anthropogenic nutrients to the coastal zone (Seitzinger et al., 2005, 2010). The autochthonous production will transform inorganic nutrients to organic while sequestering atmospheric CO_2. More importantly, rivers also deliver dissolved organic carbon (DOC) and particulate organic carbon (POC) to the coastal ocean, which can be remineralized and released as CO_2 to the atmosphere. Until recently, most global-ocean biogeochemistry models omitted or poorly represented riverine point sources of nutrients and carbon. Lacroix et al. (2020) added yearly-constant riverine loads to the ocean surface layer on a coarse resolution (1.5°) model. They assessed that CO_2 outgassing from river loads accounted for ~10% of the global ocean CO_2 sink. We anticipate that the implementation of DPR forcing and higher-resolution grids in ESMs and ECCO biogeochemical state estimates (ECCO-Darwin, Carroll et al., 2020) will help better resolve the global carbon budget (Friedlingstein et al., 2019).

LOAC development has historically had a low priority in OGCMs, ESMs, and GODAPs, and the exchange of freshwater between rivers/estuaries and the coastal ocean has been previously neglected. Our results demonstrate that the representation of runoff forcing in ECCO simulations is a major source of bias for coastal SSS. Our improvements and sensitivity analysis of river runoff in ECCO will directly contribute to: (i) the evaluation, understanding, and improvement of river-dominated coastal margins in global-ocean circulation models, (ii) investigation of mechanisms that drive seasonal and interannual variability in coastal plume processes, and (iii) bridge the gap between land-ocean interactions. These efforts will ultimately help to resolve land-ocean-atmosphere processes and feedbacks in next-generation earth system models better.

Code and Data Availability

The MITgcm and user manual are available from the project website: http://mitgcm.org/. The ECCOv4 setup can be found at http://wwwcvs.mitgcm.org/viewvc/MITgcm/MITgcm_contrib/llc_hires/. The exact version of MITgcm, ECCOv4 configuration, MATLAB routines to process the ECCOv4 output, generate the target model skill assessment diagram, and produce the paper figures are archived on Zenodo (doi:10.5281/zenodo.4106405). The SMAP observations can be downloaded from http://apdrc.soest.hawaii.edu/las/v6/dataset?catitem=2928. The model forcing and simulated salinity fields at different resolutions are archived on Zenodo (doi:10.5281/zenodo.4095613).

Author Contribution

Dimitris Menemenlis designed the experiments and Hong Zhang carried them out. Dimitris Menemenlis, Hong Zhang, Dustin Carroll, and Yang Feng developed the model code. Yang Feng prepared the manuscript with contributions from Huijie Xue, Dustin Carrol, Yan Du, and Hui Wu.

Acknowledgment

The work was supported by CAS Pioneer Hundred Talents Program Startup Fund (Y9SL11001); Southern Marine Science and Engineering Guangdong Laboratory (Guangzhou) (GML2019ZD0303, 2019BT2H594), ISEE2018PY05 from Chinese Academy of Sciences; the Chinese Academy of Sciences (XDA15020901; 133244KYSB20190031), the National Natural Science Foundation of China (41830538 and 42090042), and Guangdong Key Laboratory of Ocean Remote Sensing (South China Sea Institute of Oceanology Chinese Academy of Sciences) (2017B030301005-LORS2001). D.M., D.C., and H.Z., carried out research at Jet Propulsion Laboratory, California Institute of Technology, under contract with NASA, with grants from Biological Diversity, Physical Oceanography, and Modeling, Analysis, and Prediction Programs.

References

Adcroft, A., and Campin, J.-M., Rescaled height coordinates for accurate representation of free-surface flows in ocean circulation models, Ocean Modelling, 7(3), 269-284, doi:10.1016/j.ocemod.2003.09.003, 2004

Adcroft, A., Campin, J.-M. Hill, C. and Marshall, J., Implementation of an Atmosphere–Ocean General Circulation Model on the Expanded Spherical Cube, Monthly Weather Review, 132(12), 2845-2863, doi:10.1175/MWR2823.1, 2004

Banas, N. S., MacCready, P. and Hickey, B. M., The Columbia River plume as cross-shelf exporter and along-coast barrier, Continental Shelf Research, 29(1), 292-301, doi:10.1016/j.csr.2008.03.011.,2009

Barichivich, J., Gloor, E., Peylin, P., Brienen, R. J. W., Schöngart, J., Espinoza, J. C., and Pattnayak, K. C., Recent intensification of Amazon flooding extremes driven by strengthened Walker circulation, Science Advances, 4(9), eaat8785, doi:10.1126/sciadv.aat8785.,2018

Bentsen, M., The Norwegian Earth System Model, NorESM1-M - Part 1: Description and basic evaluation of the physical climate, Geoscientific. Model Development, 6, 687-720, doi:10.5194/gmd-6-687-2013.,2013

Bourgeois, T., Resplandy, J. C. Orr, L., Terhaar, J., Ethé, C., Gehlen, M. and Bopp, L., Coastal-ocean uptake of anthropogenic carbon, Biogeosciences, 13(14), 4167-4185, doi:10.5194/bg-13-4167-2016.,2016

Campin, J.-M., Marshall, J. and Ferreira, D., Sea ice–ocean coupling using a rescaled vertical coordinate z*, Ocean Modelling, 24, 1-14, doi:10.1016/j.ocemod.2008.05.005., 2008

Carroll, D., Menemenlis, Adkins, J.F., Bowman, K.W., Brix, H., Dutkiewicz, S., Gierach, M. M., Hill, C., Jahn, O., Landschützer, P., Lauderdale, J. Liu, J.M., Naviaux, J.D., Manizza, M., Rödenbeck, C., Schimel, D. S., Van der Stocken, T., and Zhang, (2020) H, Seasonal to Multi-decadal Air-sea CO2 Fluxes from the Data-constrained ECCO-Darwin Global Ocean Biogeochemistry Model, Journal of Advances in Modeling Earth Systems, Accepted

Chao, S. -Y., River-forced estuarine plumes. Journal of Physical Oceanography., 18, 72 – 88. doi:10.1175/1520-0485(1988)018<0072:RFEP>2.0.CO;2, 1988

Chao, S. -Y., Wind-driven motion of estuarine plumes, Journal of Physical Oceanography, 18, 1144-1166. doi:10.1175/1520-0485(1988)018<1144:WDMOEP>2.0.CO;2; 1988

Cione, J. J., and Uhlhorn, E. W. Sea surface temperature variability in hurricanes: Implications with respect to intensity change. Monthly Weather Review. 1783-1796, doi:10.1175/2562.1; 2003

Cochrane, J. D., Kelly, F. J., Low-frequency circulation on the Texas-Louisiana continental shelf. J. Geophys. Res. 91(C9), 10645-10659.,1986

de Boyer Montégut, C., Madec, G., Fischer, A. S., Lazar, A. & Ludicone, D, Mixed layer depth over the global ocean: An examination of profile data and a profile-based climatology, 109(C12), doi:10.1029/2004jc002378.,2004

Denamiel, C., Budgell, W. P. & Toumi, R, The Congo River plume: Impact of the forcing on the far-field and near-field dynamics, Journal of Geophysical Research-Oceans, 118, 964–989, doi:10.1002/jgrc.20062.,2013

Du, Y., & Zhang, Y., Satellite and Argo Observed Surface Salinity Variations in the Tropical Indian Ocean and Their Association with the Indian Ocean Dipole Mode. J. Climate, 28, 695–713, doi:10.1175/JCLI-D-14-00435.1.,2015

Fekete, B. M., Vörösmarty, C. J. and Grabs, W, High-resolution fields of global runoff combining observed river discharge and simulated water balances, 16(3), 15-11-15-10, doi:10.1029/1999gb001254.,2002

Fennel, K., et al. Carbon cycling in the North American coastal ocean: a synthesis, Biogeosciences, 16(6), 1281-1304, doi:10.5194/bg-16-1281-2019.,2019

Fennel, K., Hu, J., Laurent, A., Marta-Almeida, M., & Hetland, R. Sensitivity of hypoxia predictions for the northern Gulf of Mexico to sediment oxygen consumption and model nesting. Journal of Geophysical Research: Oceans, 118, 990–1002. doi:10.1002/jgrc.20077., 2013

Feng, Y., DiMarco, S. F., Balaguru, K., and Xue, H. Seasonal and interannual variability of areal extent of the Gulf of Mexico hypoxia from a coupled physical-biogeochemical model: A new implication for management practice. Journal of Geophysical Research: Biogeosciences, 124,1939–1960. doi:10.1029/2018JG004745.,2019

Fong, D. A., and Geyer, W. R., Response of a river plume during an upwelling favorable wind event, Journal of Geophysical Research-Oceans, 106(C1), 1067-1084, doi:10.1029/2000jc900134., 2001

Fong, D. A., and Geyer, W. R., The Alongshore Transport of Freshwater in a Surface-Trapped River Plume, Journal of Physical Oceanography, 32(3), 957-972, doi:10.1175/1520-0485(2002)032<0957:TATOFI>2.0.CO;2, 2002

Forget, G., Campin, J. M., Heimbach, P., Hill, C. N., Ponte, R. M. and Wunsch, C., ECCO version 4: an integrated framework for non-linear inverse modeling and global ocean state estimation, Geoscientific Model Development, 8(10), 3071-3104, doi:10.5194/gmd-8-3071-2015, 2015

Fournier, S., Reager, J. T., Lee, T., Vazquez-Cuervo, J., David, C.H., and Gierach, M. M., SMAP observes flooding from land to sea: The Texas event of 2015, Geophysical Research Letter, 43, L070821, doi:10.1002/2016GL070821, 2016

Fournier, S., Lee, T. and Gierach, M. M., Seasonal and interannual variations of sea surface salinity associated with the Mississippi River plume observed by SMOS and Aquarius, Remote Sensing of Environment, 180, 431 – 439. doi:10.1016/j.rse.2016.02.050, 2016

Fournier, S., Vialard, J., Lengaigne, M., Lee, T., Gierach, M. M., and Chaitanya, A. V. S. Modulation of the Ganges-Brahmaputra river plume by the Indian Ocean dipole and eddies inferred from satellite observations. Journal of Geophysical Research: Oceans, 122, 9591–9604. doi:10.1002/2017JC013333, 2017

Fournier, S., Vandemark, D., Gaultier, L., Lee, T., Jonsson, B., and Gierach, M. M. Interannual variation in offshore advection of Amazon-Orinoco plume waters: Observations, forcing mechanisms, and impacts. Journal of Geophysical Research: Oceans, 122, 8966–8982. doi:10.1002/2017JC013103, 2017

Fournier, S., Reager, J. T., Dzwonkowski, B., and Vazquez-Cuervo, J. Statistical mapping of freshwater origin and fate signatures as land/ocean “regions of influence” in the Gulf of Mexico. Journal of Geophysical Research: Oceans, 124, 4954–4973. doi:10.1029/2018JC014784, 2019

Friedlingstein, P., et al., Global Carbon Budget 2019, Earth System Science Data, 11, 1783-1838, doi:10.5194/essd-11-1783-2019., 2019

García Berdeal, I., B. M. Hickey, and M. Kawase, Influence of wind stress and ambient flow on a high discharge river plume, 107(C9), 13-11-13-24, doi:10.1029/2001jc000932.,2002

Garvine, R.W., Penetration of buoyant coastal discharge onto the continental shelf: a numerical model experiment. Journal of Physical. Oceanography. 29, 1892–1909. doi:10.1175/1520-0485(1999)029<1892:POBCDO>2.0.CO;2,1999

Garvine, R. W. The impact of model configuration in studies of buoyant coastal discharge. Journal of Marine Research. 59, 193-225. doi:10.1357/002224001762882637, 2001

Gaspar, P., Grégoris, Y. & Lefevre, J.-M., A simple eddy kinetic energy model for simulations of the oceanic vertical mixing: Tests at station Papa and long-term upper ocean study site, 95(C9), 16179-16193, doi:10.1029/JC095iC09p16179, 1990

Gent, P. and Mcwilliams, J.: Isopycnal mixing in ocean circulation models, J. Phys. Oceanogr., 20, 150–155, 1990.

Gierach, M. M., Vazquez-Cuervo, J., Lee, T., and Tsontos, V. M., Aquarius and SMOS detect effects of an extreme Mississippi River flooding event in the Gulf of Mexico, Geophysical Research Letter, 40, L50995. doi:10.1002/grl.50995, 2013

Griffies, S. M., et al., Formulation of an ocean model for global climate simulations, Ocean Science, 1(1), 45-79, doi:10.5194/os-1-45-2005. 2005

Griffies, S. M., Gnanadesikan, A. Pacanowski, R. C., Larichev, V. D., Dukowicz, J. K. and Smith, R.D. Isoneutral Diffusion in a z-Coordinate Ocean Model, *Journal of Physical Oceanography* 28, 5 (1998): 805-830, doi:10.1175/1520-0485(1998)028<0805:IDIAZC>2.0.CO;2, 1998

Halliwell, G. R., Evaluation of vertical coordinate and vertical mixing algorithms in the HYbrid-Coordinate Ocean Model (HYCOM), Ocean Modelling, 7(3), 285-322, doi:10.1016/j.ocemod.2003.10.002.,2004

Herzfeld, M., Methods for freshwater riverine input into regional ocean models, Ocean Modelling, 90, 1-15, doi:10.1016/j.ocemod.2015.04.001.,2015

Huang, R. X., Real Freshwater Flux as a Natural Boundary Condition for the Salinity Balance and Thermohaline Circulation Forced by Evaporation and Precipitation, Journal of Physical Oceanography, 23(11), 2428-2446, doi:10.1175/1520-0485(1993)023<2428:RFFAAN>2.0.CO;2, 1993

Kourafalou, V. H., Oey, L.-Y., Wang, J. D., and Lee, T. N., The fate of river discharge on the continental shelf: 1. Modeling the river plume and the inner shelf coastal current, *Journal of Geophysical Research*, 101(C2), 3415– 3434, doi:10.1029/95JC03024.,1996

IPCCs, Climate Change and Land: an IPCC special report on climate change, desertification, land degradation, sustainable land management, food security, and greenhouse gas fluxes in terrestrial ecosystems [P.R. Shukla, J. Skea, E. Calvo Buendia, V. Masson-Delmotte, H.-O. Pörtner, D. C. Roberts, P. Zhai, R. Slade, S. Connors, R. van Diemen, M. Ferrat, E. Haughey, S. Luz, S. Neogi, M. Pathak, J. Petzold, J. Portugal Pereira, P. Vyas, E. Huntley, K. Kissick, M. Belkacemi, J. Malley, (eds.)]. In press. 2019

Jolliff, J. K., Kindle, J. C., Shulman, I., Penta, B., Friedrichs, M. A. M., Helber, R. and Arnone, R. A., Summary diagrams for coupled hydrodynamic-ecosystem model skill assessment, Journal of Marine Systems, 76(1), 64-82, doi:10.1016/j.jmarsys.2008.05.014., 2009

Lacroix, F., Ilyina, T. and Hartmann, J., Oceanic CO2 outgassing and biological production hotspots induced by pre-industrial river loads of nutrients and carbon in a global modeling approach, Biogeosciences, 17(1), 55-88, doi:10.5194/bg-17-55-2020.,2020

Landschützer, P., Gruber, N. and Bakker, D. C. E., Decadal variations and trends of the global ocean carbon sink, Global Biogeochemical Cycles, 30(10), 1396-1417, doi:10.1002/2015GB005359.,2016

Landschützer, P., Laruelle, G. G., Roobaert, A., and Regnier, P.: A uniform pCO2 climatology combining open and coastal oceans, Earth Syst. Sci. Data Discuss., doi: 10.5194/essd-2020-90, in review, 2020

Lentz, S. J., The Amazon River plume during AMASSEDS: subtidal current variability and the importance of wind forcing. Journal of Geophysical Research – Oceans, 100, 2377–2390, doi:10.1029/94JC00343, 1995a

Lentz, S. J., Seasonal variations in the horizontal structure of the Amazon plume inferred from historical hydrographic data. Journal of Geophysical Research-Oceans, 100, 2391–2400, doi:10.1029/94JC01847, 1995b

Liang, L., Xue, H., & Shu, Y. (2019). The Indonesian throughflow and the circulation in the Banda Sea: A modeling study. Journal of Geophysical Research: Oceans, 124. doi:10.1029/2018JC014926

Liao, X., Du, Y., Wang, T., Hu, S., Zhan, H., Liu, H. and Wu, G., High-Frequency Variations in Pearl River Plume Observed by Soil Moisture Active Passive Sea Surface Salinity, Remote Sensing, 12, 563, doi:10.3390/rs12030563, 2020

Liu, Y., MacCready, P. and Hickey, B. M., Columbia River plume patterns in summer 2004 as revealed by a hindcast coastal ocean circulation model, Geophysical Research Letter, 36, L02601, doi:10.1029/2008GL036447.,2009

Marshall, J., Adcroft, A., Hill, C., Perelman, L. and Heisey, C., A finite-volume, incompressible Navier Stokes model for studies of the ocean on parallel computers, 102(C3), 5753-5766, doi:10.1029/96jc02775.,1997

Mecklenburg, S., Drusch, M., Kerr, Y. H., Font, J., Martin-Neira, M., Delwart, S., . . . Crapolicchio, R. ESA’s soil moisture and ocean salinity mission: Mission performance and operations. IEEE Transactions on Geoscience and Remote Sensing, 50, 1354–1366. Doi:10.1109/TGRS.2012.2187666.,2012

Menemenlis, D., Hill, C. N., Adcroft, A. J., Campin, J.-M., Cheng, B., Ciotti, R. B., . . . Zhang, J. NASA Supercomputer Improves Prospects for Ocean Climate Research. EOS Transactions AGU 86, 89–96. Doi:10.1029/2005EO090002,2005

Menemenlis, D., Campin, J.-M., Heimbach, P., Hill, C. N., Lee, T., Nguyen, A. T., . . . Zhang, H. ECCO2: High Resolution Global Ocean and Sea Ice Data Synthesis. Mercator Ocean Quarterly Newsletter, 31, 13–21.,2008

Meng, Z., Ning, L. Yuping G., & Yang, F. Exchanges of surface plastic particles in the South China Sea through straits using Lagrangian method, Journal of Tropical Oceanography, 39, 109-116. doi:10.11978/2019118 (In Chinese with English Abstract)

Molleri, G.S.F., Novo, E. M. L. M. & Kampel, M. Space-time variability of the Amazon River plume based on satellite ocean color, Continental Shelf Research, 30, 342-352. doi:10.1016/j.csr.2009.11.015, 2010

Neetu, S., Lengaigne, M., Vincent, E. M., Vialard, J., Madec, G., Samson, G., . . . Durand, F. Influence of upper-ocean stratification on tropical cyclones-induced surface cooling in the Bay of Bengal. Journal of Geophysical Research-Oceans, 117, C12020, doi:10.1029/2012JC008433,2012

Palma, E. D., & Matano, R. P., An idealized study of near equatorial river plumes,J. Geophys. Res. Oceans,122, 3599–3620, doi:10.1002/2016JC012554, 2017

Piecuch, C. G., & Wadehra, R. Dynamic sea level variability due to seasonal river discharge: A preliminary global ocean model study. Geophysical Research Letters, 47, e2020GL086984. Doi:10.1029/2020GL086984,2020

Rao, R. R., and Sivakumar, R. Seasonal variability of the salt budget of the mixed layer and near-surface layer salinity structure of the tropical Indian Ocean from a new global ocean salinity climatology. Journal of Geophysical Research-Oceans, 108, 3009. doi:10.1029/2001JC000907, 2003

Resplandy, L., Keeling, R.F., Rödenbeck, C., Stephens, B.B., Khatiwala, S., Rodgers, K.B., Long, M.C., Bopp, L., Tans, P.P., Revision of global carbon fluxes based on a reassessment of oceanic and riverine carbon transport. Nature Geoscience 1. doi: 10.1038/s41561-018-0151-3,2018

Roobaert, A., Laruelle, G. G. Landschützer, P., Gruber, N., Chou, L. and Regnier, P., The Spatiotemporal Dynamics of the Sources and Sinks of CO2 in the Global Coastal Ocean, Global Biogeochemical Cycles, 33(12), 1693-1714, doi:10.1029/2019GB006239,2019

Roullet, G., and Madec, G., Salt conservation, free surface, and varying levels: A new formulation for ocean general circulation models, 105(C10), 23927-23942, doi:0.1029/2000jc900089.,2000

Santini, M., and Caporaso, L. Evaluation of freshwater flow from rivers to the sea in CMIP5 simulations: Insights from the Congo River basin. Journal of Geophysical Research: Atmospheres, 123, 10,278–10,300. Doi:10.1029/2017JD027422,2018

Schiller, R. V., and Kourafalou, V. H., Modeling river plume dynamics with the HYbrid Coordinate Ocean Model, Ocean Modelling, 33(1), 101-117, doi:10.1016/j.ocemod.2009.12.005.,2011

Seitzinger, S. P., Harrison, J. A., Dumont, E., Beusen, A. H. W., and Bouwman, A. F., Sources and delivery of carbon, nitrogen, and phosphorus to the coastal zone: An overview of Global Nutrient Export from Watersheds (NEWS) models and their application, Global Biogeochemical Cycles, 19, GB4S01, doi:10.1029/2005GB002606.,2005

Seitzinger, S. P., Mayorga, E., Bouwman, A. F., Kroeze, C., Beusen, A. H. W., Billen, G., Drecht, G. V., Dumont, E., Fekete, B. M., Garnier, J., and Harrison, J. A. Global river nutrient export: A scenario analysis of past and future trends, Global Biogeochemical Cycles., 24, GB0A08, doi:10.1029/2009GB003587.,2010

Sengupta, D., Goddalehundi, B. R., and Anitha, D. S. Cyclone-induced mixing does not cool SST in the post-monsoon North Bay of Bengal. Atmospheric Science Letters, 9, 1–6. Doi:10.1002/asl.162.,2008

Stammer, D., Ueyoshi, K., Köhl, A. Large, W.G., Josey, S. A., and Wunsch, C., Estimating air-sea fluxes of heat, freshwater, and momentum through global ocean data assimilation, Journal of Geophysical Research, 109(C5), doi:10.1029/2003jc002082.,2004

Su, Z., Wang, J., Klein, P., Thompson, A. F. and Menemenlis, D., Ocean sub mesoscales as a key component of the global heat budget, Nature Communications, 9, 775, doi:10.1038/s41467-018-02983-w.,2018

Suzuki, T., Yamazaki, D., Tsujino, H., Komuro, Y., Nakano, H., and Urakawa, S., A dataset of continental river discharge based on JRA-55 for use in a global ocean circulation model, Journal of Oceanography, 74(4), 421-429, doi:10.1007/s10872-017-0458-5.,2018

Timmermann, R., Danilov, S., Schröter, J., Böning, C., Sidorenko, D., and Rollenhagen, K., Ocean circulation and sea ice distribution in a finite element global sea ice–ocean model, Ocean Modelling, 27(3), 114-129, doi:10.1016/j.ocemod.2008.10.009.2009

Tseng, Y.-h., Bryan, F. O. and Whitney, M. M., Impacts of the representation of riverine freshwater input in the community earth system model, Ocean Modelling, 105, 71-86, doi:10.1016/j.ocemod.2016.08.002.,2016

Tsujino, H., et al., JRA-55 based surface dataset for driving ocean–sea-ice models (JRA55-do), Ocean Modelling, 130, 79-139, doi:10.1016/j.ocemod.2018.07.002.,2018

Volodin, E. M., Dianskii, N. A. and Gusev, A. V., Simulating present-day climate with the INMCM4.0 coupled model of the atmospheric and oceanic general circulations, Izvestiya, Atmospheric and Oceanic Physics, 46(4), 414-431, doi:10.1134/S000143381004002X, 2010

Vialard, J., and Delecluse, P. An OGCM study for the TOGA decade. Part I: Role of salinity in the physics of the western Pacific fresh pool. Journal of Physical Oceanography, 28, 1071–1088. doi:10.1175/1520-0485(1998)028<1071:AOSFTT>2.0.CO;2, 1998

Vinaychandran, P., Murty, V. S. N., and Ramesh Babu, V. Observations of barrier layer formation in the Bay of Bengal during summer monsoon. Journal of Geophysical Research-Oceans, 107, 8018. Doi:10.1029/2001JC000831,2002

Walker, N. D. Satellite assessment of Mississippi River plume variability: causes and predictability, Remote Sensing of Environment, 58, 21-35. doi:10.1016/0034-4257(95)00259-6,1996

Ward, N.D., Megonigal, J.P., Bond-Lamberty, B. *et al.* Representing the function and sensitivity of coastal interfaces in Earth system models. *Nature Communicaitons* **11,** 2458 (2020). https://doi.org/10.1038/s41467-020-16236-2.

Willmott, C. J., On the validation of models, Phys. Geogr., 2, 184–194, doi:10.1080/02723646.1981.10642213.,1981

Yueh, S. H., Tang, W., Fore, A. G., Neumann, G., Hayashi, A., Freedman, A., . . . Lagerloef, G. S. L-band passive and active microwave geophysical model functions of ocean surface winds and applications to Aquarius retrieval. IEEE Transactions on Geoscience and Remote Sensing, 51, 4619–4632. doi:10.1109/TGRS.2013.2266915, 2013

Yueh, S. H., Tang, W., Fore, A., Hayashi, A., Song, Y. T., and Lagerloef, G. Aquarius geophysical model function and combined active passive algorithm for ocean surface salinity and wind retrieval. Journal of Geophysical Research: Oceans, 119, 5360–5379. doi:10.1002/2014JC009939, 2014

Zhang, H., Menemenlis, D. and Fenty, G. ECCO LLC270 Ocean-Ice State Estimate. doi:1721.1/119821,2018

Zweng, M.M, Reagan, J.R., Seidov, D., Boyer, T.P., Locarnini, R.A., Garcia, H.E., Mishonov, A.V., Baranova, O.K., Weathers, K.W., Paver, C.R. and Smolyar, I.V. World Ocean Atlas 2018, Volume 2: Salinity. A. Mishonov, Technical Editor, NOAA Atlas NESDIS 82, 50pp., 2019

Aman, A. A., Cman, C., and Bman, B. B.: More test articles, J. Adv. Res., 35, 13–28, doi:10.2345/67890, 201